POLITECNICO DI TORINO
Repository ISTITUZIONALE

Bimodal Operation of High-Contrast Gratings: The Generalized Fabry-Pérot Perspective

Original
Bimodal Operation of High-Contrast Gratings: The Generalized Fabry-Pérot Perspective / Tibaldi, A., Debernardi, P., Orta, R.. - ELETTRONICO. - (2019), pp. 3812-3816. (2019 PhotonIcs & Electromagnetics Research Symposium - Spring (PIERS-Spring) Roma 17-20 giugno 2019) [10.1109/PIERS-Spring46901.2019.9017611].

Availability:
This version is available at: 11583/2800634 since: 2020-03-05T11:45:20Z

Publisher:
IEEE

Published
DOI:10.1109/PIERS-Spring46901.2019.9017611

Terms of use:

This article is made available under terms and conditions as specified in the corresponding bibliographic description in the repository

Publisher copyright
IEEE postprint/Author's Accepted Manuscript

©2019 IEEE. Personal use of this material is permitted. Permission from IEEE must be obtained for all other uses, in any current or future media, including reprinting/republishing this material for advertising or promotional purposes, creating new collecting works, for resale or lists, or reuse of any copyrighted component of this work in other works.

(Article begins on next page)

08 November 2026

Bimodal Operation of High-Contrast Gratings: the Generalized Fabry-Pérot Perspective

A. Tibaldi[1], **P. Debernardi**[2], **and R. Orta**[1,2]

[1]Dipartimento di Elettronica e Telecomunicazioni, Politecnico di Torino, Corso Duca degli Abruzzi 24, 10129 Torino (TO), Italia

[2]Istituto di Elettronica e di Ingegneria dell'Informazione e delle Telecomunicazioni (IEIIT), Consiglio Nazionale delle Ricerche (CNR), Corso Duca degli Abruzzi 24, 10129 Torino (TO), Italia

Abstract— Previous works ascribe the broadband high-reflectivity features of high-contrast gratings (HCGs) to dual-mode interference effects occurring in the grating bars, which are a characteristic of their near-wavelength operation regime. Using this fundamental characteristic this work exploits a bimodal Fabry-Pérot interferometer approach to better understand the HCG physics. This analytic framework allows to explain the 100 % reflectivity peaks at the basis of the broadband operation, predicting their positions by closed-form expressions. A design strategy based on this approach is then presented, including a discussion on the impact of fabrication tolerances on the HCG performance.

1. INTRODUCTION: HIGH-CONTRAST GRATING REFLECTORS

Already dominating the market of short-range data communications, in the last few years the production of vertical-cavity surface-emitting lasers (VCSELs) is experiencing a boom after their successful integration in smartphones [1, 2, 3]. In this context, one of the hottest R&D topics is the design of VCSELs featuring tunable emission wavelength, whose commercialization could represent a breakthrough in telecom, sensing or biomedical applications [4, 5]. In such devices, the tuning mechanism is based on varying the cavity length by moving one of the mirrors, which makes its volume and weight fundamental design parameters. Polarization control is very important as well, in order to guarantee a stable response over the tuning range. This is why, fifteen years after their first presentation [6], high-contrast gratings (HCGs) are still a topical research subject.

A HCG is a periodic array of dielectric bars with refractive index n_1 (commonly a semiconductor) surrounded by a medium with much lower index n_2 (usually air, or an oxide). This is shown in Fig. 1 (left), which reports all the HCG design parameters: the thickness t_g, the period Λ, and the duty cycle η, defined as the ratio of the bar width to the period. HCGs can be designed as single-polarization ultrabroadband reflectors, as shown in Fig. 1 (right), which shows the reflectivity spectrum of a HCG reflector for a normal incidence TM-polarized plane wave operating in the mid-IR range [7].

HCGs operate at wavelengths comparable to Λ, in the so-called near-wavelength regime. In such condition, neither the approximations valid for sub-wavelength gratings nor diffraction theory are applicable, and a reliable analysis must rely on full-wave simulations. A possible simulation strategy is based on fully numerical approaches such as finite difference [8], finite element [9], or spectral element [10, 11] methods, which allow to model structures with complex geometries but do not provide any insight on their principle of operation or on design rules. On the other hand, these dielectric periodic structures lend themselves to modal methods such as the rigorous coupled wave analysis (RCWA) [12, 7, 10, 13].

Aiming to understand and predict the reflectivity features of HCGs we developed a generalization of the Fabry-Pérot interferometer [14, 15, 16]. In the next section, after reviewing its fundamental concepts, analytic expressions predicting the position of 100 % reflection peaks are reported. A novel design strategy relying on the very fast computations allowed by this framework is finally presented.

2. HCGS AS BIMODAL FABRY-PÉROT INTERFEROMETERS

The red curve reported in Fig. 1 (right) shows the reflectivity R in natural scales, which is very flat. In order to better appreciate the reflectivity variations, a blue curve has been inserted, which reports the same information, scaled in number of nines:

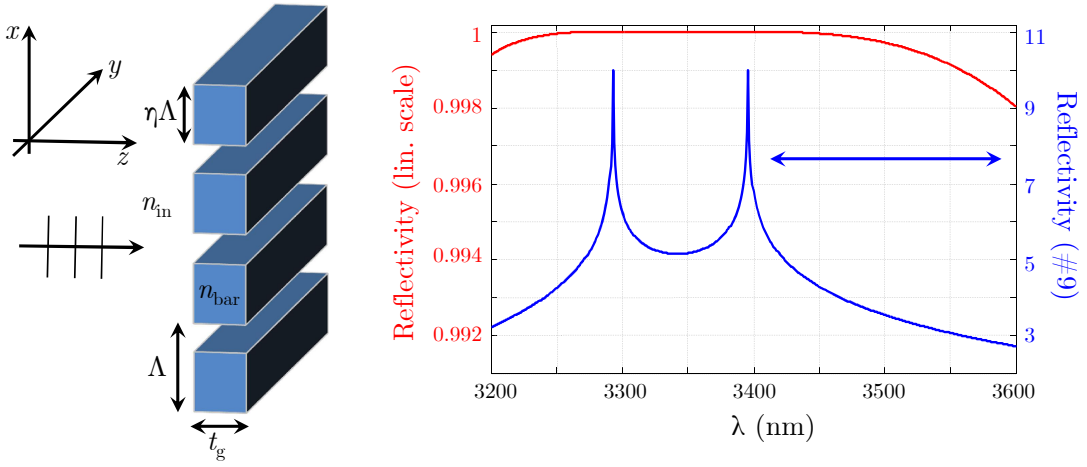

Figure 1: Left: sketch of a high-contrast grating, including the relevant geometrical parameters. Right: normal incidence TM reflectivity spectrum in linear (red curve) and in number of nines (blue curve) scales of the HCG having $n_1 = 3.6$, $n_2 = 1$, $\Lambda = 1.425\,\mu$m, $t_g = 0.865\,\mu$m, $\eta = 75\,\%$.

$$R^{\#9} = -\log_{10}(1-R).$$

The presence of two strong reflectivity peaks, which delimit the high reflectivity band, can be noticed at a glance. Since the mirror performance strongly depends on the relative positions of these peaks, they deserve a deeper investigation.

By studying the intermediate results of the RCWA simulations used to trace these curves, it can be noticed that the distinctive feature of the HCG near-wavelength regime is the presence of two propagating modes in the grating bars and one Floquet mode in the homogeneous half-spaces surrounding them [17]. On this basis, it is possible to establish an analogy between HCGs and bimodal Fabry-Pérot interferometers [14]. Figure 2 shows the circuit representation of a bimodal FPI. The cavity, which models the bar region, supports two modes, represented by two transmission lines having length t_g and propagation constants k_1, k_2. For the sake of simplicity, the transmission line parameters adopted in the formulation have been written in terms of common mode and differential phase shifts:

$$\overline{\vartheta} = \frac{k_1 + k_2}{2} t_g \qquad\qquad \Delta\vartheta = (k_1 - k_2) t_g.$$

The transmission line couplings at the bar-air interfaces are described by unitary symmetric 3×3 scattering matrices, under the hypothesis of lossless reciprocal junctions. Focusing on the right junction, the following parametrization can be obtained [14]:

$$\begin{aligned}
\overline{S}_{11} &= \mathrm{e}^{-\mathrm{j}(\varphi_c+\Delta)} \left[\mathrm{e}^{\mathrm{j}\Psi}\cos^2\Phi\cos\Theta - \mathrm{e}^{-\mathrm{j}\Psi}\sin^2\Phi\right] \\
\overline{S}_{22} &= \mathrm{e}^{-\mathrm{j}(\varphi_c-\Delta)} \left[\mathrm{e}^{-\mathrm{j}\Psi}\cos^2\Phi - \mathrm{e}^{\mathrm{j}\Psi}\sin^2\Phi\cos\Theta\right] \\
\overline{S}_{12} &= \frac{1}{2}\mathrm{j}\mathrm{e}^{-\mathrm{j}\varphi_c}\sin 2\Phi \left[\mathrm{e}^{-\mathrm{j}\Psi} + \mathrm{e}^{\mathrm{j}\Psi}\cos\Theta\right] \\
\overline{S}_{13} &= \mathrm{j}\mathrm{e}^{\mathrm{j}\frac{-\varphi_c+\varphi_{33}+\Psi}{2}}\mathrm{e}^{-\mathrm{j}\frac{\Delta}{2}}\sin\Theta\cos\Phi \\
\overline{S}_{23} &= -\mathrm{e}^{\mathrm{j}\frac{-\varphi_c+\varphi_{33}+\Psi}{2}}\mathrm{e}^{\mathrm{j}\frac{\Delta}{2}}\sin\Theta\sin\Phi \\
\overline{S}_{33} &= \mathrm{e}^{\mathrm{j}\varphi_{33}}\cos\Theta.
\end{aligned} \tag{1}$$

Here, 1 and 2 identify the ports inside the cavity, and 3 is the accessible one. By inspecting the S_{i3} expressions it is possible to provide an immediate physical interpretation of some of the parameters. In fact, Θ and φ_{33} characterize the magnitude and phase of the reflection coefficient seen from the outer port, while Φ controls the partitioning of the transmitted power between ports 1 and 2. Not so obvious interpretations can be gained for the remaining parameters: Ψ plays a relevant role in the magnitude of the $\overline{S}_{11}$, $\overline{S}_{22}$ and $\overline{S}_{12}$ coefficients, while φ_c and Δ are related to the positions of the reference planes of ports 1 and 2. A unique feature of this parametrization is the possibility to

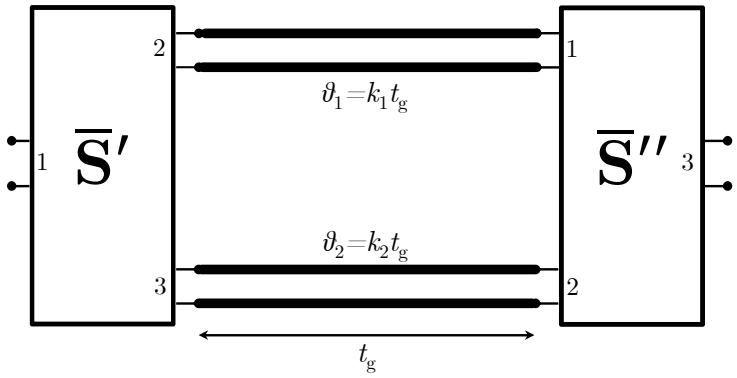

Figure 2: Equivalent circuit of a bimodal FPI. The left and right scattering matrices are connected through two transmission lines having length t_g and propagation constants k_1, k_2.

obtain explicit inverse formulas enabling the bimodal FPI model identification with HCGs without resorting to optimization methods [14].

This framework allows to demonstrate rigorously that the peaks in Fig. 1 (right) are 100% reflectivity points. In fact, closed-form expressions of the bimodal FPI reflection and transmission coefficients S_{11} and S_{21} can be achieved by defining the equivalent transmission line parameters

$$\overline{\vartheta}_{\mathrm{eq}} = \overline{\vartheta} + \varphi_{\mathrm{c}} \qquad\qquad \Delta\vartheta_{\mathrm{eq}} = \Delta\vartheta + 2\Delta$$

and computing the cascade of the scattering matrices parametrized according to (1). Focusing on the transmission coefficient, it can be compactly written as

$$S_{21} = \frac{N_{21}}{D} \mathrm{e}^{-\mathrm{j}\overline{\vartheta}_{\mathrm{eq}}} \mathrm{e}^{\mathrm{j}\varphi_{33}}.$$

In absence of losses, 100 % reflection is equivalent to zero transmission, which corresponds to $N_{21} = 0$. Since N_{21} can be written as

$$N_{21} = -\frac{1}{2} \mathrm{e}^{-\mathrm{j}(\Psi + \Delta\vartheta_{\mathrm{eq}}/2)} \sin^2\Theta \left(c_{0\mathrm{n}} + c_{1\mathrm{n}} \mathrm{e}^{-\mathrm{j}2\overline{\vartheta}_{\mathrm{eq}}} \right),$$

where

$$c_{0\mathrm{n}} = \mathrm{e}^{\mathrm{j}2\Psi} \left(1 - \mathrm{e}^{\mathrm{j}\Delta\vartheta_{\mathrm{eq}}} + \left(1 + \mathrm{e}^{\mathrm{j}\Delta\vartheta_{\mathrm{eq}}} \right) \cos 2\Phi \right)$$
$$c_{1\mathrm{n}} = \left(1 - \mathrm{e}^{\mathrm{j}\Delta\vartheta_{\mathrm{eq}}} \right) - \left(1 + \mathrm{e}^{\mathrm{j}\Delta\vartheta_{\mathrm{eq}}} \right) \cos 2\Phi,$$

the transmission zero occurs if

$$\overline{\vartheta}_{\mathrm{eq,z}} = -\Psi + \arctan\left(\frac{\tan(\Delta\vartheta_{\mathrm{eq}}/2)}{\cos 2\Phi} \right). \tag{2}$$

This result can be exploited to formulate novel HCG design guidelines. In fact, the junction parameters (1) exhibit a very mild wavelength dependence, so that they can be evaluated by RCWA just at few wavelengths and interpolated over the whole operation range. Evaluating the explicit expressions of the transmission coefficient and its zeros enables a complete HCG parameter space exploration with negligible computational costs. The huge exploration output dataset can be synthesized in Fig. 3 (left), which reports the transmission zero loci for gratings with bar refractive index $n_1 = 3.214$ surrounded by air versus wavelength and duty cycle. Each locus is obtained for a different grating thickness t_g. It is to be remarked that determining each $(\lambda/\Lambda, \eta)$ point of the loci, without the approach described in this work, would require inserting the RCWA in an optimization loop, leading to thousands of RCWA evaluations. On the contrary, this map has been obtained in few seconds on a standard personal computer.

Figure 3 (left) can be used to design the grating thickness and duty cycle simply by inspection, while the period can be determined from the central operation wavelength. In fact, the HCG bandwidth and reflectivity levels are strongly related to the position of the transmission zeros:

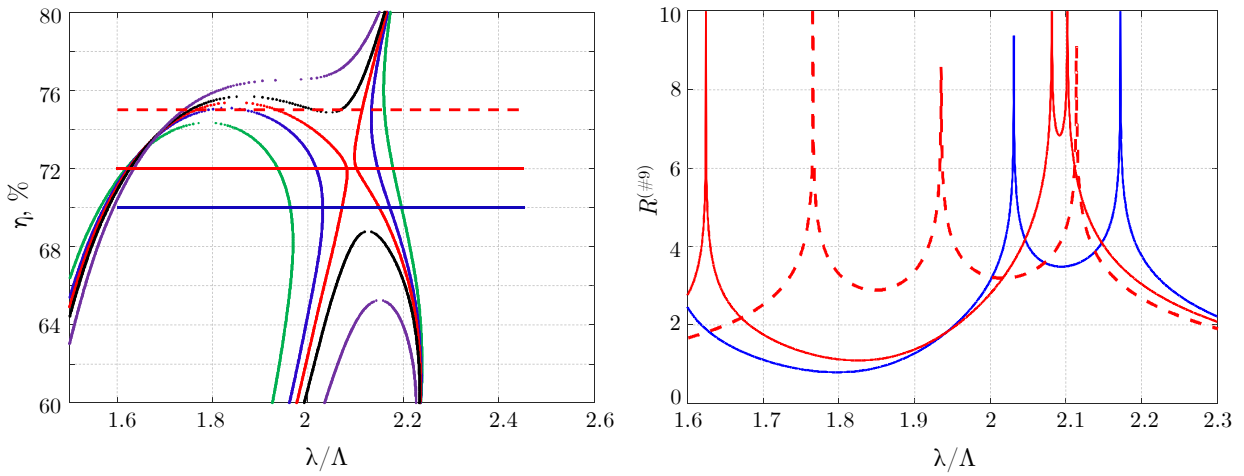

Figure 3: Left: transmission zero loci of HCGs having $n_1 = 3.214$, $n_2 = 1$. Each curve corresponds to a different grating thickness t_g: $0.619\,\Lambda$ (green), $0.629\,\Lambda$ (blue), $0.633\,\Lambda$ (red), $0.637\,\Lambda$ (black), $0.647\,\Lambda$ (purple). Right: reflectivity spectra, in number of nines, corresponding to the horizontal cuts reported in the left plot.

close zeros lead to very high reflectivity over narrow bands, and vice versa. To demonstrate this point, Fig. 3 (right) shows the TM plane-wave reflectivity spectra for three designs. Each design corresponds to one of the horizontal cuts in the left figure, and the color indicates which locus is intersected. In particular, the solid red curve is obtained for $t_g = 0.633\Lambda$ and $\eta = 72\,\%$, for which the transmission zeros are very close and reflectivity is around 99.99999%. The solid blue curve is obtained for $t_g = 0.629\Lambda$ and $\eta = 70\,\%$: the zeros are more distant, and reflectivity is higher than $99.9\,\%$ over a broader band compared to the previous design. Both these designs are based on the idea of *intersecting* a region of Fig. 3 (left) where the transmission zero loci are almost vertical. In this view, an alternative could be to select a duty cycle such that the zero loci are more or less horizontal, leading in this example to the ultrabroadband HCG design reported with the dashed red line.

The synthetic parameter space representation allows also to perform a qualitative sensitivity analysis. In fact, a tolerance on the duty cycle introduces a vertical shift of the zero loci intersections, while the effect of a non-ideal grating thickness can be estimated by interpolating the different loci. In this view, the ultrabroadband design is very sensitive on duty cycle, since minor variation could lead to no zero loci intersections. On the other hand, the other designs prove to be much more robust.

3. CONCLUSIONS

This work deals with the design-oriented analysis of high-contrast grating reflectors. A generalization of the Fabry-Pérot interferometer concept to the bimodal case is presented, with the aim of mimicking the dual-mode interference phenomena occurring in the HCG bars. Explicit expressions of the generalized interferometer response can be achieved, thanks to the novel parametrization of 3×3 unitary symmetric matrices, applied to the bar-air interfaces scattering matrices. This approach enables very fast explorations of the HCG design parameter space, supporting the formulation of a new design strategy, which is applied to some design examples.

REFERENCES

1. R. Michalzik, Ed., *VCSELs: Fundamentals, Technology and Applications of Vertical-Cavity Surface-Emitting Lasers*. Berlin: Springer-Verlag, 2013.
2. H. Moench, M. Carpaij, P. Gerlach, S. Gronenborn, R. Gudde, J. Hellmig, J. Kolb, and A. van der Lee, "VCSEL based sensors for distance and velocity," in *Proc. SPIE 9766*, Mar. 2016, pp. 97 660A–1–16.
3. K. J. Ebeling, R. Michalzik, and H. Moench, "Vertical-cavity surface-emitting laser technology applications with focus on sensors and three-dimensional imaging," *Japan. J. Appl. Phys.*, vol. 52, pp. 08PA02–1–11, 2018.
4. C. Gierl, T. Gruendl, P. Debernardi, K. Zogal, C. Grasse, H. A. Davani, G. Böhm, S. Jatta, F. Küppers, P. Meißner, and M.-C. Amann, "Surface micromachined tunable 1.55 μm-VCSEL

with 102 nm continuous single-mode tuning," *Opt. Express*, vol. 19, no. 18, pp. 17 336–17 343, Aug. 2011.

5. D. D. John, C. B. Burgner, B. Potsaid, M. E. Robertson, B. K. Lee, W. J. Choi, A. E. Cable, J. G. Fujimoto, and V. Jayaraman, "Wideband electrically pumped 1050-nm MEMS-tunable VCSEL for ophtalmic imaging," *J. Lightwave Technol.*, vol. 33, no. 16, pp. 3461–3468, 2015.
6. C. F. R. Mateus, M. C. Y. Huang, Y. Deng, A. R. Neureuther, and C. J. Chang-Hasnain, "Ultrabroadband mirror using low-index cladded subwavelength grating," *IEEE Photon. Technol. Lett.*, vol. 16, no. 2, pp. 518–520, 2004.
7. A. Tibaldi, P. Debernardi, and R. Orta, "High-contrast grating performance issues in tunable VCSELs," *IEEE J. Quantum Electron.*, vol. 51, no. 12, p. 2400407, 2015.
8. A. Taflove and S. C. Hagness, Eds., *Computational electrodynamics: the finite-difference time-domain method*, 3rd ed. Norwood, MA: Artech House, 2005.
9. G. Pelosi, A. Freni, and R. Coccioli, "Hybrid technique for analysing scattering from periodic structures," *IEE Proc.-Microw. Antennas Propag.*, vol. 140, no. 2, pp. 65–70, 1993.
10. R. H. Morf, "Exponentially convergent and numerically efficient solution of Maxwell's equations for lamellar gratings," *J. Opt. Soc. Amer. A*, vol. 12, no. 5, pp. 1043–1056, 1995.
11. A. Tibaldi, R. Orta, O. A. Peverini, G. Addamo, G. Virone, and R. Tascone, "Skew incidence plane-wave scattering from 2-D dielectric periodic structures: analysis by the mortar-element method," *IEEE Trans. Microwave Theory Tech.*, vol. 63, no. 1, pp. 11–19, 2015.
12. M. G. Moharam and T. K. Gaylord, "Rigorous coupled-wave analysis of planar-grating diffraction," *J. Opt. Soc. Amer.*, vol. 71, no. 7, pp. 811–818, July 1981.
13. M. Dems, R. Kotynski, and K. Panajotov, "Planewave admittance method - a novel approach for determining the electromagnetic modes in photonic structures," *Opt. Express*, vol. 13, no. 9, pp. 3196–3207, 2005.
14. R. Orta, A. Tibaldi, and P. Debernardi, "Bimodal resonance phenomena–part I: generalized Fabry–Pérot interferometers," *IEEE J. Quantum Electron.*, vol. 52, no. 12, pp. 6 100 508–1–8, 2016.
15. ——, "Bimodal resonance phenomena–part II: high/low-contrast grating resonators," *IEEE J. Quantum Electron.*, vol. 52, no. 12, pp. 6 600 409–1–8, 2016.
16. A. Tibaldi, P. Debernardi, and R. Orta, "Bimodal resonance phenomena–part III: high-contrast grating reflectors," *IEEE J. Quantum Electron.*, vol. 54, no. 6, pp. 6 600 108–1–8, 2018.
17. C. J. Chang-Hasnain and W. Yang, "High-contrast gratings for integrated optoelectronics," *Adv. Opt. Photonics*, vol. 4, no. 3, pp. 379–440, 2012.